

The Kolmogorov-Smirnov test for the CMB

Mona Frommert,^{1,2} Ruth Durrer¹ and Jérôme Michaud¹

¹Département de Physique Théorique and Center for Astroparticle Physics,
Université de Genève, 24 quai Ernest Ansermet, CH-1211 Genève 4, Switzerland

²Max-Planck-Institut für Astrophysik,
Karl-Schwarzschild-Str. 1, 85741 Garching, Germany

E-mail: mona.frommert@unige.ch

Abstract. We investigate the statistics of the cosmic microwave background using the Kolmogorov-Smirnov test. We show that, when we correctly de-correlate the data, the partition function of the Kolmogorov stochasticity parameter is compatible with the Kolmogorov distribution and, contrary to previous claims, the CMB data are compatible with Gaussian fluctuations with the correlation function given by standard Λ CDM. We then use the Kolmogorov-Smirnov test to derive upper bounds on residual point source power in the CMB, and indicate the promise of this statistics for further datasets, especially Planck, to search for deviations from Gaussianity or for point sources.

Keywords: CMB, non-gaussianity

1 Introduction

The cosmic microwave background (CMB) is the most precise, best understood and therefore also most precious dataset in cosmology. Within the accuracy of present observations, the CMB exhibits a perfect blackbody spectrum of radiation at the temperature $T_0 = (2.72548 \pm 0.00057)\text{K}$ [1] with small, Gaussian fluctuations and a tiny amount of polarisation. The anisotropies and the polarisation can to a large extent be calculated within linear perturbation theory. Therefore, if the initial conditions are Gaussian as predicted from simple inflationary models, the temperature anisotropies and the polarisation should represent Gaussian random fields in the sky.

In this paper we outline a new method to test the Gaussianity of the CMB sky using the well-known Kolmogorov-Smirnov test. We describe how to de-correlate Gaussian variables so that the Kolmogorov-Smirnov test can be applied. We also discuss in detail practical issues one has to deal with when applying the Kolmogorov-Smirnov test to CMB data. Such practical issues include finite-size effects, numerical issues for highly correlated data, effects from determining the covariance matrix from the same dataset which is to be de-correlated, and correlations between different subsets of the CMB map for which we compute the Kolmogorov stochasticity parameter. Not taking into account these effects can lead to wrong conclusions about the result of the Kolmogorov-Smirnov test. Once all of these issues are taken into account properly, the failure of the Kolmogorov-Smirnov test would be an indication that the data is non-Gaussian and it can be used to quantify higher order correlations.

When applying the Kolmogorov-Smirnov test to data from the Wilkinson Microwave Anisotropy Probe (WMAP), we find no indication of such a failure; the maps seem to be entirely compatible with Gaussian fluctuations whose correlation function is given by the standard ΛCDM model. Note, though, that since the significance of the outcome of the Kolmogorov-Smirnov test is limited by the resolution of the CMB map, this result might change with future CMB data as e.g. from the Planck satellite.

We further use the Kolmogorov-Smirnov-test to obtain upper bounds on residual point source power in the CMB. The results are not yet competitive to the WMAP constraints, but they are derived for every band separately, without assuming a given scaling of the point-source power with frequency as in the WMAP papers. There are also ways of improving these constrains, which we plan to explore in future work.

In the next Section we introduce the Kolmogorov-Smirnov test, discuss its modification for correlated variables, and study in detail different effects that can change the results of the test. In Section 3 we apply it to simulated and measured CMB data. In Section 4, we use the Kolmogorov-Smirnov test to obtain upper bounds on residual radio point sources in the CMB. In Section 5 we conclude and discuss future applications of the method outlined here.

2 The Kolmogorov-Smirnov test

2.1 Basics

The Kolmogorov-Smirnov test is based on the following mathematical theorem [2]:

Theorem: (Kolmogorov)

Let $\{X_1, \dots, X_n\}$ be n **independent** realizations of a real random variable X ordered such

that $X_1 \leq X_2 \leq \dots \leq X_n$ and be

$$F(x) = P\{X \leq x\} \quad (P = \text{probability}) \quad (2.1)$$

the partition function of X . The empirical partition function is given by

$$F_n(x) := \begin{cases} 0 & \text{if } x < X_1 \\ k/n & \text{if } X_k \leq x < X_{k+1} \\ 1 & \text{if } X_n \leq x. \end{cases} \quad (2.2)$$

The Kolmogorov stochasticity parameter is defined by

$$\lambda_n := \sqrt{n} \sup_x |F_n(x) - F(x)|. \quad (2.3)$$

Its partition function, denoted by $\Phi(n, \lambda)$,

$$\Phi(n, \lambda) = P\{\lambda_n \leq \lambda\}, \quad (2.4)$$

converges uniformly to the Kolmogorov distribution $\Phi_K(\lambda)$ given by $\Phi_K(\lambda) := 0$ for $\lambda \leq 0$ and

$$\Phi_K(\lambda) := \sum_{k=-\infty}^{k=\infty} (-1)^k \exp(-2k^2\lambda^2) \quad \text{for } \lambda > 0. \quad (2.5)$$

$$\lim_{n \rightarrow \infty} \Phi(n, \lambda) = \Phi_K(\lambda). \quad (2.6)$$

The Kolmogorov distribution, Φ_K , is independent of F .

This theorem holds whenever the partition function F is continuous.

We would like to apply the theorem to the temperature fluctuations $\Delta T(\mathbf{n})$ in different directions \mathbf{n} , but there are two conditions of the theorem which are not satisfied a priori:

First, the temperature fluctuations, even if they are a realization of the same stochastic process at each point (this is a consequence of stochastic isotropy), are not independent at different points. The CMB sky is correlated,

$$\langle \Delta T(\mathbf{n}_1) \Delta T(\mathbf{n}_2) \rangle = C(\theta) \neq 0, \quad \cos \theta = \mathbf{n}_1 \cdot \mathbf{n}_2.$$

Secondly, we do not know the theoretical distribution F of CMB anisotropies. We assume it to be Gaussian with mean zero but the variance, $C(0)$ is determined from the data. Hence we compare the data with an empirically obtained distribution F . Clearly, the Gaussian distribution F obtained by using the variance of the data will in general be closer to the empirical distribution F_n than statistically expected.

In addition, there are several practical issues such as finite-size effects and numerical issues for highly correlated data, which can change the results of the Kolmogorov-Smirnov test significantly. We discuss all of these effects in more detail in Sections 2.2 and 2.3 and in the Appendix.

In the literature the Kolmogorov-Smirnov test has been applied to the CMB without any discussion of the above-mentioned issues [4]. We believe that the conclusions drawn in these papers are not reliable because of that. Recently the first point and the issue of finite-size effects have been addressed in Ref. [5]. We shall comment on this in more detail below.

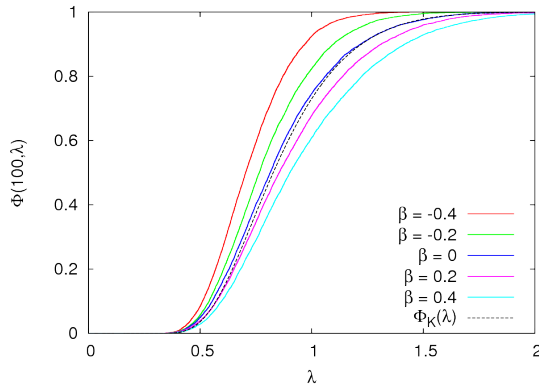


Figure 1. The partition function for λ_n as function of the correlation parameter β for $n = 100$. Curves from left to right correspond to $\beta = -0.4, -0.2, 0, 0.2, 0.4$. The curve for $\beta = 0$ (middle, dark blue) agrees with the Kolmogorov distribution $\Phi_K(\lambda)$ (dashed black line). We have used 10000 realizations of the model to explore the partition function $\Phi(100, \lambda)$ for each value of β . As we have argued above, for positive correlations the distribution function is shifted to the right (to higher values of λ_n), while it is shifted to the left for negative correlations.

2.2 Effects of correlated variables, finite-size, and empirical determination of parameters

It is not difficult to guess what correlations will do to the Kolmogorov stochasticity parameter: positive correlations will favor the variables X_j to cluster. For a fixed number n they thus explore less of the space of values than uncorrelated variables and therefore F_n is expected to deviate more from the theoretical distribution F and the Kolmogorov parameter λ_n will in general be larger. If the correlations are negative the opposite effect is expected and the stochasticity parameter λ_n is reduced.

This result is illustrated in Fig. 1, where the partition function of $\lambda_n = \sqrt{n} \sup_y |F_n(y) - F(y)|$ is shown for $n = 100$ for a model with nearest neighbor correlations,

$$\langle Y_j Y_i \rangle = \begin{cases} 0 & \text{if } |i - j| > 1 \\ \beta & \text{if } |i - j| = 1 \\ 1 & \text{if } i = j. \end{cases} \quad (2.7)$$

We draw independent random variables X_j from a Gaussian normal distribution with vanishing mean and variance one, $N(0, 1)$. The correlated variables Y_j are obtained by following the opposite of the procedure outlined in Section 2.3 below on uncorrelated variables. Another, analytically solvable model is presented in Ref. [6]. Note that throughout this paper, we will denote correlated random variables by Y_j , whereas X_j are understood to be independent variables drawn from $N(0, 1)$.

To compare with the correlated results we also show the partition function $\Phi(n, \lambda)$ for the uncorrelated variables X in the upper left panel of Fig. 2. This is useful in order to separate effects from correlations from those of finite size (i.e. small n). For $n = 100$, the finite-size effects are already very small (the curve is already very close to the Kolmogorov-curve). However, if we compute the mean of $\Phi_K(\lambda_n)$ for $n = 100$ from $m = 10000$ samples, it is $\langle \Phi_K \rangle \approx 0.48$ rather than 0.5, as we would expect for the limiting case of $n \rightarrow \infty$. This is only a difference of a few percent, however, this difference will become relevant for us later on. We study the effects of small n in much more detail in Appendix C.

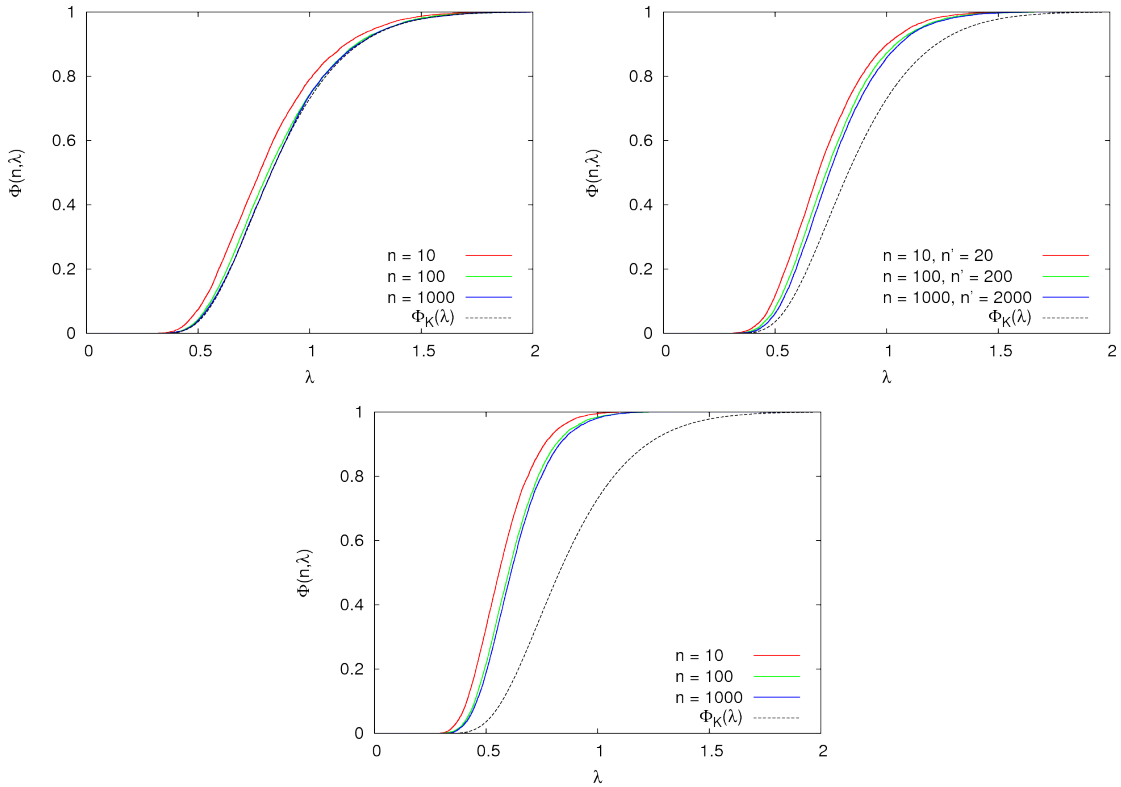


Figure 2. *Upper left:* Partition function $\Phi(n, \lambda)$ for n independent random variables X for $n = 10, 100,$ and 1000 . Superimposed is the Kolmogorov function $\Phi_K(\lambda)$. *Upper right:* $\Phi(n, \lambda)$ for n independent random variables if the partition function F is taken to be $F = N(a, b)$ where the mean a and variance b are determined from the data. The number of X_i used to determine a and b is twice the one used to compute λ_n , $n' = 2n$. *Bottom:* Same as in the middle panel, but with $n' = n$.

Intuitively it is also clear what happens if we determine the parameters of the theoretical distribution function from the data which we also use to calculate F_n : on average the distance λ_n between F_n and F will be smaller and therefore also $\Phi_K(\lambda_n)$ is smaller, see also [11]. In the upper right and bottom panels of Fig. 2, we show the partition function $\Phi(n, \lambda)$ obtained if F is not taken to be $N(0, 1)$ but $N(a, b)$ where we determine the mean a and the variance b from the data,

$$a = \frac{1}{n'} \sum_{i=1}^{n'} X(\mathbf{n}_i) \quad (2.8)$$

$$b = \frac{1}{n' - 1} \sum_{i=1}^{n'} (X(\mathbf{n}_i) - a)^2. \quad (2.9)$$

In this case, F_n is by construction too close to F , thus moving $\Phi(n, \lambda)$ to the left. This effect is quite strong if we determine the parameters from the same set of X_i that we use to compute λ_n (c.f. bottom panel of Fig. 2, where we used $n' = n$) and becomes less pronounced if we use additional X_i to compute the mean and the variance (upper right panel, $n' = 2n$).

We suspect that such an effect is the reason why the authors of Refs [4] have obtained so small values for $\Phi_K(\lambda_n)$ especially for relatively small n , see also [5]. With increasing n

the value $\Phi_K(\lambda_n)$ calculated in Refs. [4] grows, approaching unity in two cold spots with 5° radius. We suggest that this is due to the correlations of the temperature anisotropies in this region. In the next Section we shall show this quantitatively.

2.3 De-correlating Gaussian variables

Let us consider an n -dimensional Gaussian variable Y with vanishing mean but with correlations. Its probability density is then given by

$$f_Y(y) = \frac{1}{\sqrt{(2\pi)^n \det C}} \exp\left(-\frac{1}{2}y \cdot C^{-1}y\right), \quad y \in \mathbb{R}^n, \quad (2.10)$$

where C is the symmetric, positive definite correlation matrix,

$$\langle Y_i Y_j \rangle = \int d^n y y_i y_j f_Y(y) = C_{ij}. \quad (2.11)$$

We can diagonalize this matrix with some orthogonal matrix O so that

$$C = O M O^T \quad M = \begin{pmatrix} \mu_1^2 & \cdots & 0 \\ 0 & \ddots & 0 \\ 0 & \cdots & \mu_n^2 \end{pmatrix}. \quad (2.12)$$

If Y is Gaussian, the n variables X_i defined by

$$X_i = \frac{1}{\mu_i} (O^T Y)_i \quad (2.13)$$

are uncorrelated and distributed with the normal distribution $N(0, 1)$. On these variables the Kolmogorov-Smirnov test should apply, i.e., the partition function of the stochasticity parameter λ_n should converge to Φ_K for large n .

If the partition function $\Phi(n, \lambda)$ for λ_n obtained by comparing the empirical distribution of X with $N(0, 1)$ does not converge to the Kolmogorov function Φ_K there are two possibilities.

- We have not used the correct correlation matrix C (which is typically determined by the cosmological parameters).
- The fluctuations are not Gaussian, i.e. there are also higher order correlations such that even though $\langle X_i X_j \rangle = \delta_{ij}$, Wick's theorem is not satisfied for higher order correlators.

In either case this would falsify the hypothesis that CMB fluctuations are well explained by Gaussian inflationary perturbations in a Λ CDM model with the cosmological parameters inferred in the literature.

We must, however, note that even though we do determine the correlation function from the cosmological parameters and not directly from the data, these parameters are inferred using the same data and are therefore not independent of it. Also in this approach, we are therefore somewhat subject to the problem that we determine the distribution of our variables from the data itself. In Appendix A we show that for the case of the CMB we do not see this effect. The reason is that the Λ CDM model puts a strong prior on the form of the correlation function, leaving only six parameters to be determined from a large amount

of available CMB data. In addition, we then use only a small subset of these data for our Kolmogorov-Smirnov test, i.e. $n' \gg n$ in the language of Section 2.2.

Note also that the de-correlation transformation, eq. (2.13), has its limitations for very strongly correlated random variables. In the limiting case of two perfectly correlated random variables, $Y_1 = Y_2$, the covariance matrix C has one zero eigenvalue, so that we cannot compute X_i for this eigenvalue. In such a case, one needs to directly work with the correlated variables Y , and compare the partition function of their Kolmogorov parameter to simulated ones. This is what we call ‘correlation method’ in the following.¹ In cases where we do not have perfectly correlated data, but nevertheless very strong correlations (e.g. between neighbouring pixels), we can still run into numerical problems with the transformation in eq. (2.13), since we divide by a very small number μ_i . We investigate this effect for CMB maps with negligible noise in Appendix B: The empirical partition function of the Kolmogorov stochasticity parameter for the de-correlated variables can be significantly shifted to the right due to very strong correlations.

3 Application to the CMB

In this Section we apply the Kolmogorov-Smirnov test to simulated data and to the seven year CMB anisotropy data from WMAP.

3.1 Simulated data

We start by calculating the CMB correlation function using the best fit cosmological parameters of WMAP, as they are given in [8], see table 1. The last digit given is rounded and

n_s	=	0.96	scalar spectral index
Δ_R	=	2.4×10^{-9}	amplitude of the curvature perturbation spectrum
r	=	0	tensor to scalar ratio
$h^2\Omega_b$	=	0.0226	baryon density
$h^2\Omega_c$	=	0.111	cold dark matter density
τ	=	0.088	optical depth to the last scattering surface
Ω_Λ	=	0.73	cosmological constant
Ω_k	=	0	curvature parameter

Table 1. The (minimal) cosmological parameters from the WMAP seven year data [8].

is uncertain. More details about the error bars and the definition of these parameters can be found in Ref. [8]. In Fig. 3 we compare the CMB angular power spectrum obtained with these parameters with the WMAP seven year data. A definition of the CMB angular power spectrum can be found e.g. in Ref. [3]

The correlation function for the temperature anisotropy of two directions \mathbf{n}_1 and \mathbf{n}_2 in the sky can be calculated from the CMB power spectrum, see [3],

$$\langle \Delta T(\mathbf{n}_1) \Delta T(\mathbf{n}_2) \rangle = \frac{1}{4\pi} \sum_{\ell=2}^{\infty} (2\ell + 1) C_\ell P_\ell(\mathbf{n}_1 \cdot \mathbf{n}_2), \quad (3.1)$$

¹An analytical investigation of such models with perfect correlations can be found in [6].

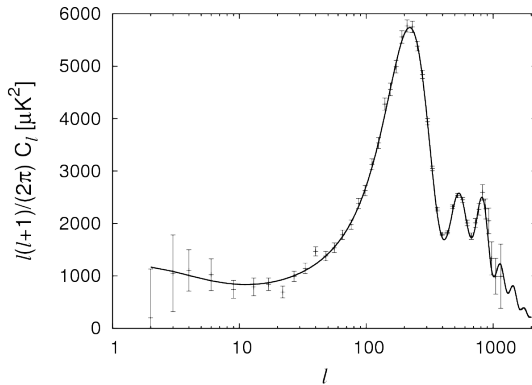


Figure 3. The C_ℓ 's from the WMAP seven year best fit cosmological parameters given above and the WMAP data with error bars.

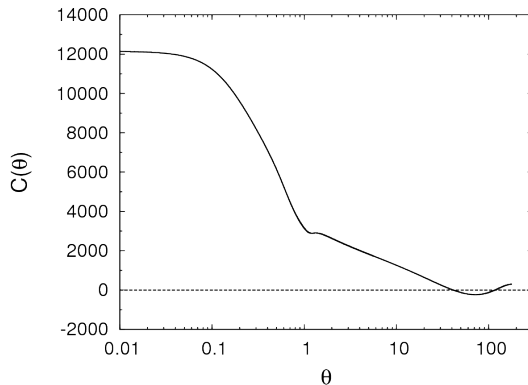


Figure 4. The CMB correlation function for the WMAP seven year best fit cosmological parameters given above in units of $(\mu K)^2$, plotted against the angle in degrees. The ‘kink’ at $\theta = 1^\circ$ corresponds to the acoustic peaks in the power spectrum.

where P_ℓ denotes the Legendre polynomial of degree ℓ . The correlation function obtained from the spectrum of Fig. 3 is shown in Fig. 4.

We now simulate datasets consisting of n CMB-‘pixels’: We draw n independent realizations $X(\mathbf{n}_i)$ from the normal distribution $N(0, 1)$, which we then correlate with the help of the correlation matrix

$$C_{ij} = C(\theta_{ij}), \quad (3.2)$$

following the opposite of the procedure outlined in Section 2.3. Here, θ_{ij} is the angular separation of the points \mathbf{n}_i and \mathbf{n}_j . For the sake of simplicity, we assume all of our data-points to lie on a great arc of opening angle α .² For a given number n of points, nearest neighbors

² Note that working with data lying on a great arc is especially useful when we consider the full circle: To transform the uncorrelated variables X to the correlated ones given by $Y_i = \mu_i(OX)_i$ where O and μ_i are defined as in Eq. (2.12), we have to diagonalize the correlation matrix C . For large values of n this requires a significant numerical investment: Diagonalization of a symmetric $n \times n$ matrix determining both, the eigenvalues μ_i^2 and the orthogonal matrix O requires n^3 operations. To sample the variable Y and therefore λ_n m times requires $\mathcal{O}(m \cdot n^3)$ operations. If however the points \mathbf{n}_i are equally spaced on a circle such that the angular separation of \mathbf{n}_1 and \mathbf{n}_n is equal to the resolution δ , the matrix C becomes ‘circulant’ and its diagonalization corresponds to a Fourier transform. In this case the number of operations can be reduced to

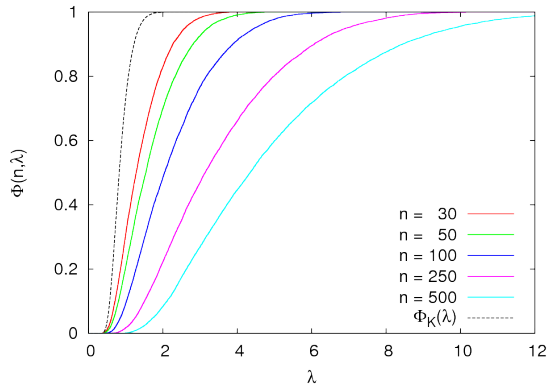


Figure 5. The partition functions $\Phi(n, \lambda)$ for n points of simulated data in a total opening angle of $\alpha = 10^\circ$ are shown for $n = 30 - 500$. For higher n the points are closer and therefore more correlated. Hence with increasing n $\Phi(n, \lambda)$ deviates more from the Kolmogorov function $\Phi_K(\lambda)$. As explained in the text, positive correlations prefer larger values of λ . The Kolmogorov function Φ_K is also indicated (dashed black line).

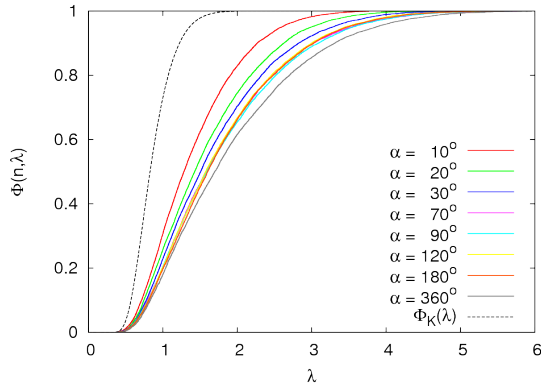


Figure 6. The partition functions $\Phi(n, \lambda)$ for n points of simulated data at fixed resolution $\delta = \alpha/n = 20$ arc minutes. Until an opening angle of $\alpha = 70^\circ$, which corresponds to $n = 210$, the correlations increase with n and $\Phi(n, \lambda)$ moves to the right, preferring larger values of λ . For larger angular separation the anti-correlations present for angular separations $50^\circ \lesssim \theta \lesssim 100^\circ$ come in and balance the correlations, such that $\Phi(n, \lambda)$ is kept at roughly the same position up to an opening angle of $\alpha = 180^\circ$. For $\alpha = 360^\circ$, corresponding to $n = 1080$, the correlations have moved $\Phi(n, \lambda)$ further to the right again. The Kolmogorov function Φ_K is also indicated (dashed black line).

then have an angular separation $\delta = \alpha/n$ and we have to include at least $\ell_{\max} > n\pi/\alpha$ C_ℓ 's in Eq. (3.1) in order to be able to resolve this scale. In practice, we use $\ell_{\max} = 2000$ for the plots in this Section.³⁴ For these CMB datasets, we obtain the partition function $\Phi(n, \lambda)$ of λ_n from 10000 simulated datasets of n ‘pixels’ each.

In Fig. 5 we show the partition functions $\Phi(n, \lambda)$ of the temperature fluctuations for

$\mathcal{O}(m \cdot n \log(n))$ which is of course a significant improvement. For more details see [6].

³Even though for $n = 250$ and $n = 500$ and an opening angle of $\alpha = 10^\circ$, $\ell_{\max} = 2000$ is not enough to completely resolve these scales, the result that a higher resolution of the map yields larger values of λ_n is not affected by this.

⁴In all of the following sections, we include the beam of the WMAP-experiment, which cuts off power at $\ell \sim 500/700/900$ for the Q/V/W-band, respectively.

points on a great arc with fixed total opening angle $\alpha = 10^\circ$ for different values of n . As the number of points, n , increases, the angular distance between nearest neighbors, $\delta = \alpha/n$, decreases and they are more and more correlated, see Fig. 4. As we have explained in Section 2, this means that the probability for higher values of λ_n becomes larger and hence the function Φ is shifted to the right with respect to the Kolmogorov function Φ_K which is also indicated as the dashed line in Fig. 5. Therefore, if in a fixed patch the number of points is increased, the typical value of λ_n increases and with it $\Phi_K(\lambda_n)$. At this level, this has nothing to do with non-Gaussian features of the CMB but is simply an effect of correlations.

In Fig. 6 we fix the resolution to $\delta = 20$ arc minutes and simply increase the number of points. In this case, the variation of $\Phi(n, \lambda)$ with n is much less pronounced. Here it comes from the fact that the total opening angle $\alpha = n\delta$ depends on n . For $n \leq 210$, which corresponds to $\alpha \leq 70^\circ$, the function Φ is still moving to the right with increasing n , i.e., correlations are becoming stronger; while for $210 < n < 540$, i.e. for $70^\circ < \alpha < 180^\circ$ the small anti-correlations which are present for angles $50^\circ \lesssim \theta \lesssim 100^\circ$, see Fig. 4, balance the correlations such that the curves Φ stay at the same position, or even move slightly to the left. For $n = 1080$, corresponding to $\alpha = 360^\circ$, the correlations have moved Φ further to the right again. Note that the partition functions for $\alpha = 10^\circ$ and 20° , corresponding to $n = 30$ and $n = 60$ are still subject to effects of small n , which shifts their partition functions to the left.

3.2 WMAP - local analysis

3.2.1 Adaption of the analysis to WMAP data

In the last Section we have studied the partition function $\Phi(n, \lambda)$ for ring segments of a given opening angle of a simulated CMB map. Here we want to analyze the observed data. For convenience we work again with ring segments of the CMB maps, so that we can readily compare our results to the simulations described in Section 3.1. Note, though, that it is straightforward to do this analysis using other subsets of a CMB map such as patches, for example. In the following we denote a λ_n computed locally for a given ring segment consisting of n pixels by λ_n^{loc} , as opposed to the global λ_n , which we introduce in Section 3.3. The λ_n^{loc} of the individual ring segments obviously contains information about whether the pixels in the respective ring segment are Gaussian and well described by the given correlation function. This could turn out to be useful for detecting local non-Gaussianities such as Galactic foregrounds, see also [4, 5]. In order to locally apply the Kolmogorov-Smirnov test to the data of the WMAP satellite, some additional steps have to be performed.

a) Choice of ring segments:

First, we modify our analysis for data that do not lie on a great arc, but on a circle in a plane parallel to the Galactic plane, characterized by an angle Θ_{ring} in Galactic coordinates. With this we can directly use the data from the WMAP temperature maps in the HEALPix ‘ring’ format. This has the advantage that we do not need to rotate the map in order to obtain data on a great arc that lies well above the Galactic plane (rotating the maps introduces significant uncertainties in the data).

From these rings, we choose segments of an opening angle of 20° and a given gap angle between the segments, in order to reduce correlations between them (both angles are measured with respect to the centre of the coordinate system). We choose the gap between the ring segments and between different rings to be 1° each. In Appendix D, we verify with

simulations that for such a gap we do not yet see any effects from correlations between the different ring segments.⁵

In order to obtain as many ring segments as possible, we use all rings between $\Theta_{\text{ring}} = 20^\circ - 60^\circ$ with a distance of 1° . We discard all pixels with point sources masked by the WMAP extended mask. If in a ring segment more than 10% of the pixels are masked, we discard the whole ring segment, thus obtaining $m = 712$ ring segments. Due to the pixelisation scheme, the number of pixels contained in a given opening angle depends on the ring. For an opening angle of 10° , the number of pixels we use varies between $n = 132$ and $n = 150$ for $\Theta_{\text{ring}} = 20^\circ - 60^\circ$. Furthermore, the masking of the pixels changes the number of pixels in a given ring segment. The variation in n causes small differences between the simulated partition functions of the λ_n for the ‘correlation method’ introduced below. However, we have verified numerically that this effect is negligible compared to the variation we obtain due to the finite number of ring segments we can extract from the map. For the simulations, we use the average number of pixels in the ring segments, $n = 143$.

b) Beam and detector noise:

When computing the correlation function from the CMB power spectrum, we need to take into account the beam transfer function of WMAP. This cuts off power at high ℓ , and it significantly reduces the power even in the first peak, see e.g. [7]. Note that the correlation function shown in Fig. 4 is computed without taking into account the WMAP beam.

Finally, we need to take into account the detector noise of WMAP. If we assume that the maps have been perfectly cleaned from Galactic foregrounds and point sources, the data (i.e. the pixels of a given ring segment) are given by

$$Y_i = \Delta T_i + n_i, \quad (3.3)$$

where ΔT_i and n_i denote the CMB temperature and the detector noise in pixel i , respectively. If we ignore small non-Gaussianities coming e.g. from inflation, the data are Gaussian distributed, with the covariance matrix

$$C_{ij} = \langle Y_i Y_j \rangle = \langle \Delta T_i \Delta T_j \rangle + N_{ij}, \quad (3.4)$$

where $\langle \Delta T_i \Delta T_j \rangle$ is the CMB correlation function shown in Fig. 4, and N is the diagonal noise covariance matrix

$$N_{ij} = \langle n_i n_j \rangle = \sigma_i^2 \delta_{ij}. \quad (3.5)$$

Here, $\sigma_i^2 = \sigma_0^2 / N_{\text{obs}}(i)$ is the detector noise variance in pixel i , which goes down with the number of observations of a given pixel, $N_{\text{obs}}(i)$ ⁶.

c) Application

We now have two possibilities to apply the Kolmogorov-Smirnov test to the WMAP data: We can either de-correlate the pixels in the ring segments using Eq. (2.13) and compare the λ_n to the Kolmogorov distribution $\Phi_K(\lambda)$. Or we can directly work with the (correlated) temperature values in the CMB map and compare to our simulated partition functions $\Phi(n, \lambda)$ of a correlated signal plus noise.

⁵We expect correlations between ring segments to manifest themselves in too steep curves for $\Phi(n, \lambda)$: Correlated ring segments ‘know about each other’, which should make the λ_n for the different ring segments more similar to each other, and thus the cumulative distribution for the λ_n steeper.

⁶ σ_0 for every frequency band can be found at http://lambda.gsfc.nasa.gov/product/map/dr4/skymap_info.cfm

method		Q	V	W
local (ring segments)	mean $[\Phi_K(\lambda_n^{\text{loc}})]$	0.496	0.497	0.483
	stddev $[\Phi_K(\lambda_n^{\text{loc}})]$	0.295	0.295	0.289
global	mean $[\Phi_K(\lambda_n)]$	0.508	0.505	0.500
	stddev $[\Phi_K(\lambda_n)]$	0.291	0.284	0.284

Table 2. Empirical mean and standard deviation of $\Phi_K(\lambda_n)$. *Top:* local analysis (de-correlation method), $n \approx 143$, $m = 712$. *Bottom:* global analysis, $n = 2000$, $m = 500$. The empirical mean should be Gaussian distributed around $\langle \Phi_K \rangle = 0.484$ (0.495) with a standard deviation of $\sigma \approx 0.011$ (0.013) for the local analysis (the global analysis). The empirical standard deviation should be about $\sqrt{\langle (\Phi_K - \langle \Phi_K \rangle)^2 \rangle} = 1/\sqrt{12} \approx 0.29$ for both. Both analyses are fully consistent with theoretical expectations.

We will present both methods in the following. In general, we consider the ‘de-correlation method’ to be preferable over the ‘correlation method’. First of all, in this case there is no need to simulate the partition function of λ_n since it is the well-known Kolmogorov distribution. The de-correlation method is also generally more powerful than the correlation method, since it is less degenerate in the detection of the different effects that can cause a deviation from the Kolmogorov curve. Consider, for example, a dataset for which the empirical partition function of the λ_n ’s lies to the right of the Kolmogorov curve $\Phi_K(\lambda)$. This could be due to correlations or to other effects such as non-Gaussianity or to the fact that we have used a wrong $F(x)$ when computing the λ_n ’s. In simulations of correlated data, we can probably mimic this effect by using a certain correlation function. However, if the shift of the curves is not due to correlations in the data, we would in general not expect to obtain the Kolmogorov distribution when de-correlating the data with any correlation function. Furthermore, with the de-correlation method it is straightforward to account for inhomogeneous noise.

However, note that the correlation method is more stable in the case of very strongly correlated pixels. Pixels can be very strongly correlated if the noise in the CMB map is negligible. In that case, the de-correlation method can lead to highly biased results, as we show in Appendix B. If the eigenvalues of the covariance matrix are extremely close to zero, it might even not work at all. For WMAP, we do not encounter this problem, because we have enough noise power on small scales. However, for future CMB experiments, this issue might become relevant.

For both methods, we compare the results obtained from WMAP data to simulations of 100 CMB maps plus Gaussian white noise (mimicking the detector noise). For the de-correlation method, we use the correct (inhomogeneous) noise variance of the maps, whereas for the correlation method, the noise variance has been averaged over all pixels that we use in the analysis. In the correlation method, adding uncorrelated noise to the simulations of correlated data reduces the correlation of the data and thus shifts the partition function $\Phi(n, \lambda)$ to the left as compared to simulations without noise. As for the de-correlation method, the inclusion of noise just slightly broadens the scatter of the curves without introducing a bias.

We apply the Kolmogorov-Smirnov test to the foreground-cleaned seven year WMAP Q-band (40.7 GHz), V-band (61 GHz), and W-band (94 GHz) maps.

3.2.2 Results: de-correlation method

We de-correlate the data from every ring segment using Eq. (2.13), which should give us independent Gaussian random variables $X_i \sim N(0, 1)$. Then, we compute the local λ_n^{loc} for

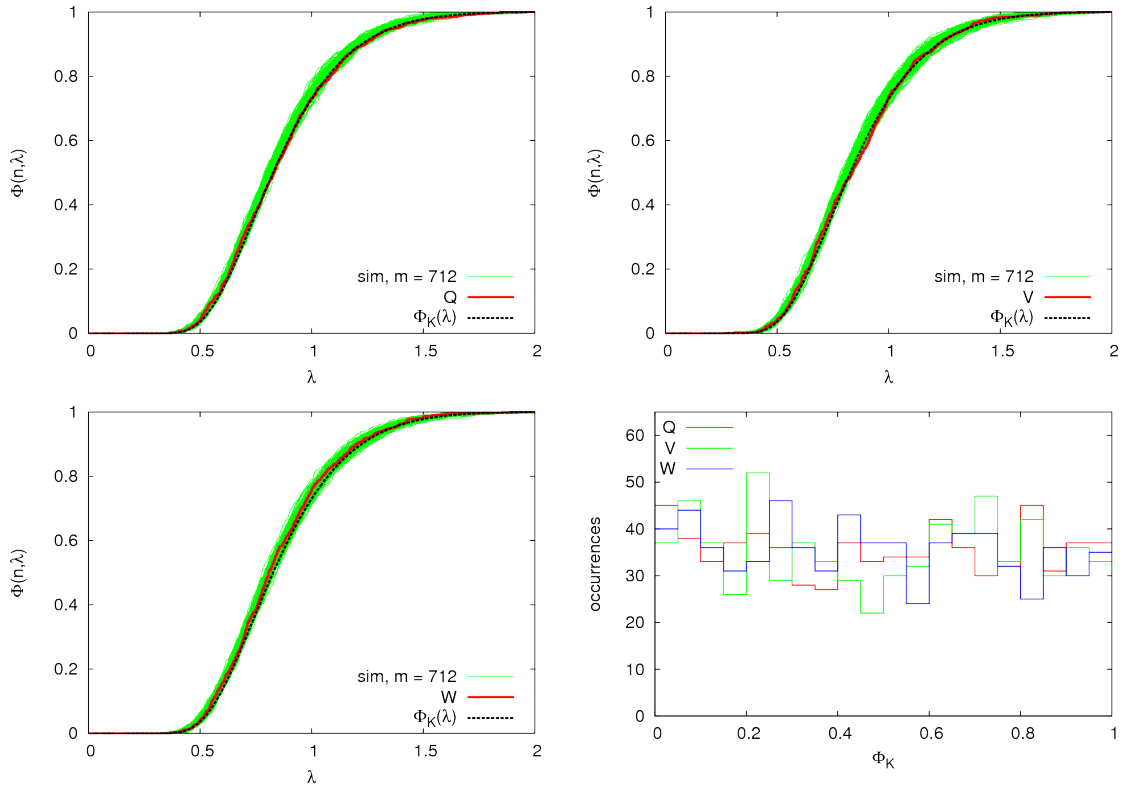


Figure 7. Decorrelation method: empirical partition function of λ_n^{loc} for WMAP-7year-data and 100 simulations for the Q-band (*upper left*), the V-band (*upper right*), and the W-band (*bottom left*). The opening angle of a given ring segment is 20° , the gap between rings and ring segments are 1° each. Pixels containing identified point sources are masked. We have $m = 712$ ring segments and on average $n = 143$ pixels per ring segment. The simulations are shown in green. *Bottom right*: histogram of Φ_K for all bands. We see a small bias towards small values of Φ_K , reflecting the effects of small n .

every ring segment. As stated above, we have between $n = 132$ and $n = 150$ pixels per ring segment to compute λ_n^{loc} , and we obtain $m = 712$ ring segments.

In order to get a visual impression of the distribution of the λ_n^{loc} of the different ring segments, we show their empirical partition function together with the Kolmogorov-curve $\Phi_K(\lambda)$ in Fig. 7. Also shown are the analysis from 100 simulated CMB maps to which Gaussian white noise has been added. For the simulations we consider homogeneous noise, whereas we account for inhomogeneous noise when de-correlating the real data. All three bands of real data lie well within the expected variance. Note that the simulated curves are biased to the left due to finite-size effects, as we show in Appendix C.

If the theoretical partition function $F(x)$ used to compute λ_n^{loc} is the correct one, the $\Phi_K(\lambda_n^{\text{loc}})$ are uniformly distributed on the interval $[0,1]$. Thus,

$$\begin{aligned} \langle \Phi_K \rangle &= 0.5, \\ \sqrt{\langle (\Phi_K - \langle \Phi_K \rangle)^2 \rangle} &= 1/\sqrt{12} \approx 0.29, \end{aligned} \quad (3.6)$$

where $\langle \cdot \rangle$ denotes an ensemble average and we have used $\Phi_K \equiv \Phi_K(\lambda_n^{\text{loc}})$ for notational simplicity. Assuming that the different Φ_K are statistically independent and using the central limit theorem, $\bar{\Phi}_K \equiv \frac{1}{m} \sum_{i=1}^m \Phi_{K,i}$ is then normally distributed around 0.5, with a standard

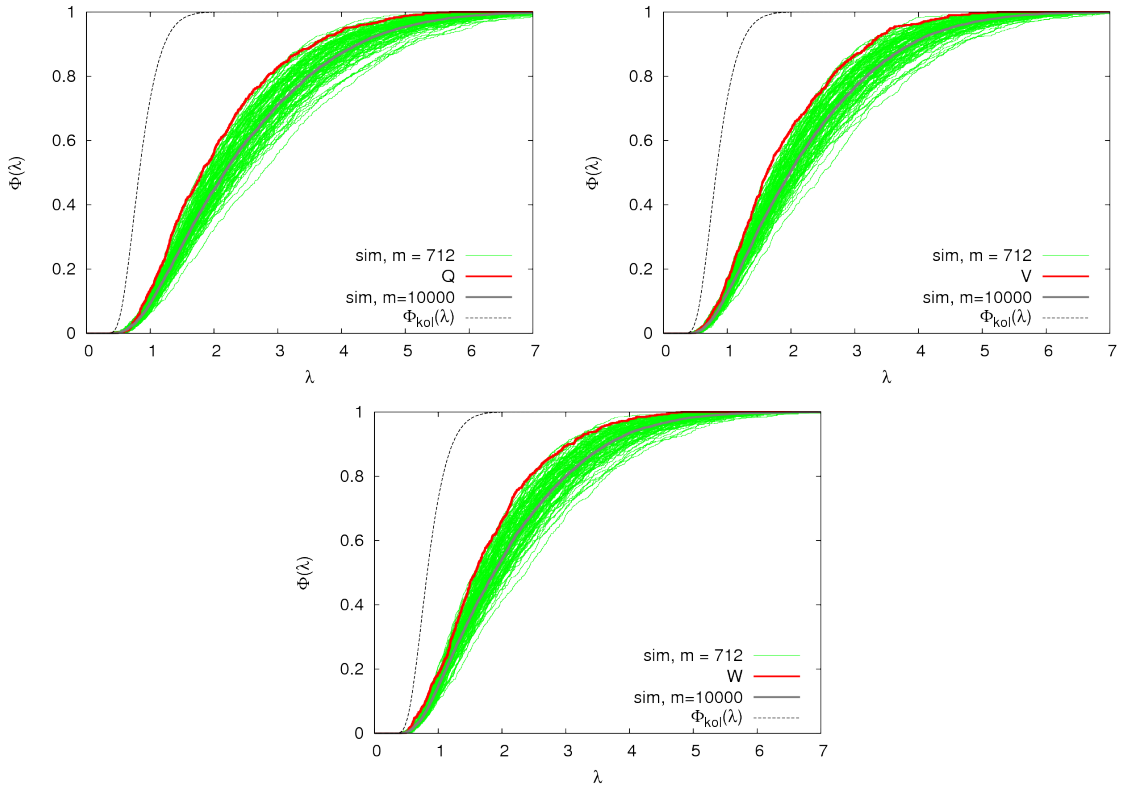


Figure 8. Correlation method: empirical partition function of λ_n^{loc} for WMAP-7year-data for the Q-, V-, and W-band (upper left, upper right, and bottom panel, respectively). We compare these to simulated partition functions $\Phi(n, \lambda)$, obtained from $m = 10000$ samples, (grey curve) and 100 realizations of $n = 143$, $m = 712$ (green curves). The opening angle of a given ring segment is 20° , the gap between rings and ring segments are 1° each. Pixels containing identified point sources are masked, and we take into account only homogeneous noise. The Kolmogorov-curve $\Phi_K(\lambda)$ is indicated by the black dashed line.

deviation of $\sigma = \frac{1}{\sqrt{12m}} \approx 0.011$ for $m = 712$. However, note that this is not quite correct for $n = 143$, due to finite-size effects, as we show in Appendix C. We show with simulations that, for $n = 143$, $\overline{\Phi_K} \equiv \frac{1}{m} \sum_{i=1}^m \Phi_{K,i}$ is distributed around 0.484 rather than around 0.5, i.e. it is biased low by about 1.5σ . In Fig. 7, we plot the histogram of Φ_K for all three bands. We do see the small bias towards small Φ_K from the finite-size effects. The values for the empirical mean and standard deviation of Φ_K are summarized in the top panel of table 2. The results are consistent with theoretical expectations.

3.2.3 Results: correlation method

Instead of de-correlating the data from the CMB map, we now directly compare the empirical partition function of λ_n^{loc} for the original correlated data with our simulated partition functions $\Phi(n, \lambda)$ for correlated data. We now consider only homogeneous noise. The effect of using the wrong noise variance in the correlation method actually introduces a bias, whereas in the de-correlation method it merely increases the scatter of the simulations. We have studied this effect by excluding the regions where the noise is most inhomogeneous, i.e. the

band	Q	V	W
mean $[\Phi_K(\lambda_n^{\text{loc}})]$	0.90	0.88	0.86
stddev $[\Phi_K(\lambda_n^{\text{loc}})]$	0.19	0.22	0.25

Table 3. Results for the three WMAP bands for the correlation method for $m = 712$ samples ($n \approx 143$): shown are the empirical mean and standard deviation of $\Phi_K(\lambda_n^{\text{loc}})$ over all ring segments. Note that now we obtain larger means for $\Phi_K(\lambda_n^{\text{loc}})$, simply because the λ_n^{loc} are larger due to the correlations between the pixels in a given ring segment. The standard deviation is smaller than 0.29, due to the flatness of the Kolmogorov-curve for large values of λ_n .

regions around the ecliptic poles, from the analysis.⁷ This left us with $m = 357$ ring segments only, rather than $m = 712$ as in the de-correlation method, thus worsening the statistical power. We found that the bias is not significantly removed by this and therefore included also the pole region in the final analysis.

The results for the different bands are shown in Fig. 8. The curves obtained from the WMAP data are still roughly consistent with the simulations, but they are now systematically too steep. This is most probably due to the fact that we only considered homogeneous noise in this analysis, while taking into account the correct noise covariance in the de-correlation method.⁸

In table 3, we show the empirical mean and standard deviation of $\Phi_K(\lambda_n^{\text{loc}})$, where Φ_K is the Kolmogorov distribution, and not the correct partition function for the correlated case. As expected, we obtain $\Phi_K(\lambda_n^{\text{loc}}) > 0.5$, simply because the λ_n^{loc} are pushed towards higher values by the correlations within the ring segments. For the typical values of $\lambda_n \sim 0.9$ we obtain, the Kolmogorov-curve is already quite flat. Thus, $\Phi_K(\lambda_n^{\text{loc}})$ varies little over the ring segments, leading to a standard deviation of Φ_K which is smaller than 0.29.

3.3 WMAP - global analysis

In order to find out whether the CMB map as a whole is Gaussian distributed and described by the correlation function used, we compute a global λ_n of the CMB map: We randomly draw $n = 2000$ pixels outside the mask from the map, de-correlate all of these pixels with their full covariance matrix (using inhomogeneous noise), and compute the global λ_n from the resulting uncorrelated data. We compute $m = 500$ of these global λ_n . The values for n and m were chosen to maximize the sensitivity of λ_n to point-source contamination, while still being safe from residual correlations between the different sets of pixels, as we explain in Section 4.

In order to get a visual impression of the results, we show the empirical partition function of λ_n , together with 20 simulated partition functions in Fig. 9. The WMAP-curves lie well within the range expected from simulations.

Just as for the local analysis in Section 3.2.2, the $\Phi_K(\lambda_n)$ have to be uniformly distributed on $[0,1]$, if all our assumptions used to compute λ_n are correct. We plot the histogram of $\Phi_K(\lambda_n)$ for $n = 2000$ and $m = 500$ for all bands in the bottom right panel of Fig. 9.

In order to obtain a more quantitative result, we again compare the empirical mean and standard deviation to the theoretical expectations, c.f. Section 3.2.2. Taking into account

⁷Around the ecliptic poles, the WMAP scanning strategy affects the structure of the noise most strongly.

⁸When considering only homogeneous noise in the de-correlation method, we also obtain curves which are less consistent with simulations than when taking into account the full noise covariance.

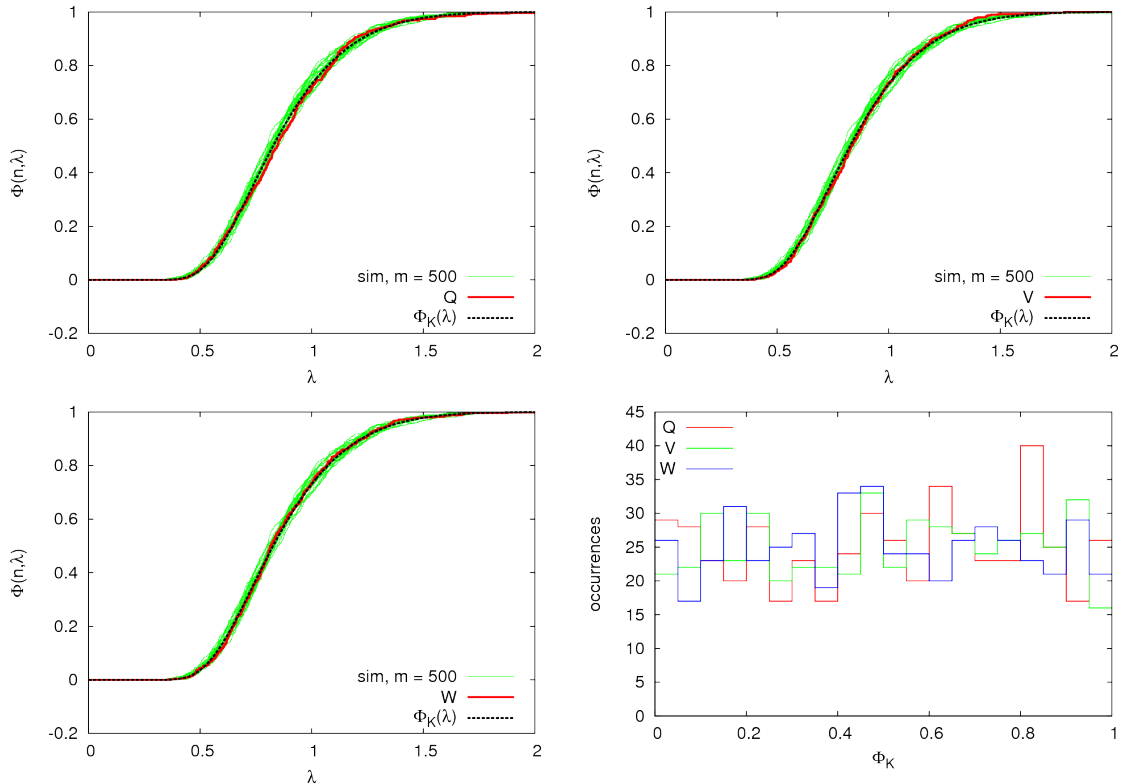


Figure 9. Global analysis: empirical partition function of λ_n^{loc} for WMAP-7year-data and 20 simulations for $m = 500$ sets of $n = 2000$ randomly drawn pixels. *Upper left: Q-band, upper right: V-band, bottom left: W-band. Bottom right panel: Histogram of Φ_K for the three bands.*

the very small bias from the effect of a finite n (c.f. Appendix C), we expect $\overline{\Phi_K}$ to be normally distributed around 0.495 with a standard deviation of $\sigma \approx 0.013$. The empirical standard deviation of Φ_K should be about 0.29. We summarize the empirical mean and standard deviation of $\Phi_K(\lambda_n)$ in table 2. The results are again fully consistent with theoretical expectations.

4 Constraints on residual point sources

One can in principle use the Kolmogorov-Smirnov test to constrain the power coming from residual (non-resolved) point sources. We consider only radio point sources, which are spatially uncorrelated (white noise) and thus have a flat power spectrum. Toffolatti et al. [10] show that the residual radio point sources are well described by a Poisson distribution. In this work, we approximate this Poisson distribution by a Gaussian, which is a good approximation if the Poisson distribution has a large mean. We can then simply add a constant contribution $C_\ell^{\text{ps}} = \text{const}$ to the CMB power spectrum and rerun the Kolmogorov-Smirnov test. We plot different point source power spectra together with the CMB power spectrum for the WMAP seven year best fit cosmological parameters in Fig. 10.

Using the spectral behaviour of the detected point sources, the frequency dependence

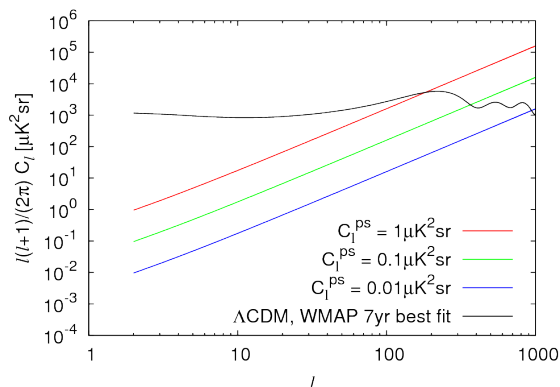


Figure 10. CMB power spectrum and 3 different constant power spectra, describing the residual point source background. The WMAP-constraints on the power spectrum of residual point sources is of the order of $0.01 \mu K^2 \text{sr}$ or better.

of C_ℓ^{ps} can be modeled as a power law [9]

$$C_\ell^{\text{ps}}(\nu) = A_{\text{ps}} r(\nu)^2 \left(\frac{\nu}{\nu_Q} \right)^{2\alpha-4}, \quad (4.1)$$

where $\alpha = -0.09$, $\nu_Q = 40.7$ GHz is the frequency of the Q-band, and $r(\nu)$ converts antenna to thermodynamic temperature:

$$r(\nu) \equiv \frac{(e^x - 1)^2}{x^2 e^x}, \quad x \equiv \frac{h\nu}{kT_{\text{cmb}}}. \quad (4.2)$$

The WMAP seven year estimate for the amplitude is $A_{\text{ps}} = (9.0 \pm 0.7) \times 10^{-3} \mu K^2 \text{sr}$ [8]. The constraints on C_ℓ^{ps} on the different bands obtained from Eq. (4.1) given this result for A_{ps} are listed in table 4.

In order to obtain constraints on the residual point sources from the Kolmogorov-Smirnov test, we add a constant point-source power spectrum to the CMB power spectrum and compute again the $m = 500$ values for the global λ_n with $n = 2000$, as in Section 3.2.2.

As we have already stated above, the values for n and m were chosen to maximize the sensitivity of λ_n to point-source contamination, while still being safe from residual correlations between the different sets of pixels: We found that the sensitivity of λ_n to a contamination of the CMB power spectrum by point sources is much higher for large n than for small n . This can be understood as follows: The effect of adding point-source power to the CMB-power spectrum is to change the partition function $F(x)$ of our de-correlated pixels. This increases the value of $\sup_x |F_n(x) - F(x)|$, c.f. equation (2.3). Now, since for large n the original supremum (without point-source power added) is smaller than for small n , it feels the change of $F(x)$ stronger (i.e. its relative change is larger than for small n). We thus chose to set $n = 2000$, for which we can still diagonalize the covariance matrix in a reasonable amount of time. In addition, for $n = 2000$ pixels, the effects from finite n are already very small, c.f. Appendix C.

The number of pixels in our map is $N_{\text{pix}} = 12 \text{nside}^2 \sim 3 \times 10^6$ for $\text{nside} = 512$. With roughly 30% of the sky masked, we are left with $\sim 2 \times 10^6$ pixels outside the mask. Therefore, every set of $n = 2000$ pixels we draw represents about 0.1% of the pixels outside the mask. If

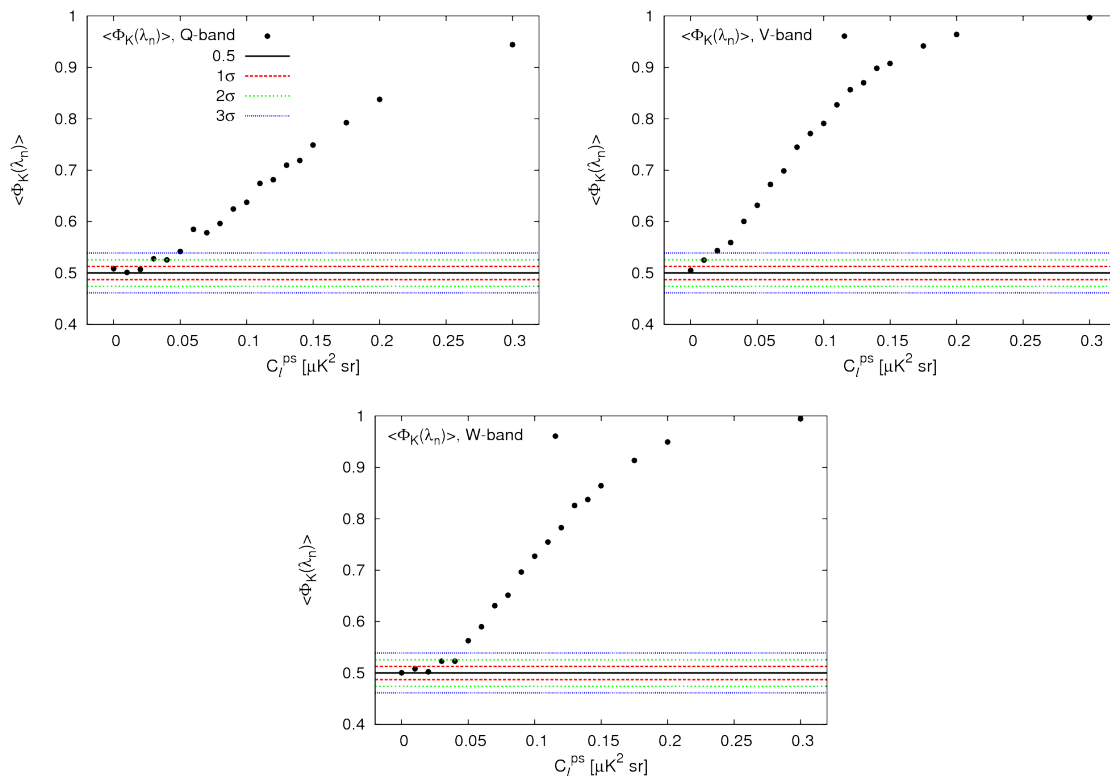


Figure 11. Empirical mean of $\Phi_K(\lambda_n)$ versus the Poisson power C_ℓ^{ps} for the Q-band (*upper left*), V-band (*upper right*), and W-band (*bottom*), for $n=2000$ and $m=500$. The confidence intervals around the expected value of 0.5 are also shown.

we draw $m = 500$ such pixel-sets, we have in total used about 50% of the pixels outside the mask (neglecting the fact that some of those might have been drawn several times). We show in Appendix D that with this we are safe from effects from residual correlations between the different pixel sets.

As in Section 3.3, we again use the fact that the empirical mean $\overline{\Phi_K}$ has to be normally distributed around 0.5 with a standard deviation of $\sigma \approx 0.013$ if we used the correct partition function F to compute λ_n .⁹ If we add too much point-source power, this hypothesis is no longer true, and $\overline{\Phi_K}$ can become very different from 0.5. We thus add point-source power C_ℓ^{ps} of different strengths to the CMB power spectrum, and plot the resulting $\overline{\Phi_K}$ versus C_ℓ^{ps} in Fig. 11. The 1σ , 2σ , and 3σ regions around the expected value of 0.5 are also shown. We obtain an upper bound on the point source power by rejecting the hypothesis if our measured value of $\overline{\Phi_K}$ lies outside the 3σ region. The bounds we obtain for every band are listed in table 4. The Q-band is affected least by the point sources, since it has the lowest resolution, and thus the beam window function cuts the higher multipoles, when the point sources are more important as compared to the CMB.

Our results obtained in this way are about 0.5 – 1 order of magnitude worse than the WMAP limits. However, note that the WMAP team has combined different bands and used an assumption about the scaling of C_ℓ^{ps} with frequency to obtain their constraints. We

⁹Note that we neglect the small bias from finite n here. This results in slightly more conservative constraints than with the bias taken into account, since $\overline{\Phi_K}$ is biased towards smaller values.

band	Q	V	W
WMAP 7 yr	$(9.8 \pm 0.8)10^{-3}$	$(2.0 \pm 0.2)10^{-3}$	$(0.43 \pm 0.03)10^{-3}$
Kol. (de-corr)	< 0.05	< 0.02	< 0.05

Table 4. Constraints on C_ℓ^{ps} in $\mu K^2 \text{sr}$ from the WMAP team and from our Kolmogorov analysis.

do not use any assumption on this and derive independent constraints for each band. We could most probably improve the constraints by using a higher n for computing λ_n , thus enhancing the sensitivity of λ_n to residual point-source power as explained above. However, as already stated above, with $n = 2000$, we are already close to the limit of what we can do with the matrix diagonalization routine we are presently using. Therefore, working with a larger n would involve using more sophisticated routines and is beyond the scope of this work. Note also that our limits are quite conservative, given that they were obtained using only 50% of the pixels outside the mask, i.e. about 35% of the sky. We could also improve our constraints by using more than 500 samples, but we would run the risk of working with correlated samples (if we were to draw the additional samples outside our current mask), or of being contaminated by Galactic foregrounds (if using a smaller mask). We prefer to be safe from these effects and thus stick to the more conservative estimate. Finally, note that we have chosen to reject the hypothesis if the data lie outside the 3σ region around the expected value, which is again quite conservative.

Given that the spherical harmonics coefficients $a_{\ell m}$ of an isotropic sky map are uncorrelated, they are probably a better choice of variables to constrain residual point source power in the map. However, this is beyond the scope of the present work, and presumably mostly useful for higher resolution maps as we expect to obtain from the Planck satellite currently taking data. These maps may make this method very competitive and certainly an interesting alternative to the standard analysis.

5 Conclusion and outlook

In this paper we have shown that the Kolmogorov stochasticity parameter of the correlated data $\Delta T(\mathbf{n})$ does not obey a Kolmogorov distribution and we have explained why this is to be expected. We have also presented a method to de-correlate the data so that the Kolmogorov-Smirnov test on the de-correlated data should give an indication whether or not the CMB anisotropies are Gaussian. Alternatively, we can apply the Kolmogorov-Smirnov test directly to the correlated data, but with a modified partition function, which takes into account the correlations and which is obtained from simulations. This latter method is to be favoured over de-correlating the data in the case of very strongly correlated data.

We have applied the Kolmogorov-Smirnov test on WMAP seven year data using both of these methods, and we have shown that the WMAP maps are fully consistent with a Gaussian dataset with the correlation function given by the best-fit cosmological parameters.

We have then used the Kolmogorov-Smirnov test to obtain conservative constraints on the constant power spectrum of residual radio point sources. With the numerical effort involved and the present resolution of the maps, our results are not compatible with the standard analysis but we are convinced that this method has considerable potential.

We plan to further explore the Kolmogorov-Smirnov test as a potential tool to test Gaussianity and to detect various types of foregrounds to the CMB.

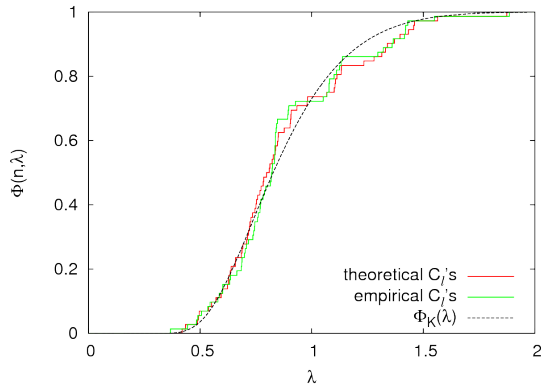


Figure 12. Empirical partition function of λ_n of simulated CMB data, de-correlated with the theoretical (i.e. correct) C_ℓ 's (red curve) and the C_ℓ 's from the best-fit Λ CDM model to the simulated data (green curve).

Acknowledgment

We thank Martin Gander, Martin Reinecke, Thomas Riller for guidance and help with numerical aspects of the project. We are grateful for discussions with Jean-Pierre Eckmann and Martin Kunz. We acknowledge the use of HEALPix [12], cmbeasy [13], and the WMAP data ¹⁰. This work is supported by the Fonds National Suisse.

A Effect of the empirical determination of the data variance for a Λ CDM model

The power spectrum used to de-correlate the data and to perform the simulations of the correlated data, has been determined as the best-fit power spectrum for the Λ CDM cosmological model from the CMB maps themselves [8]. Therefore, we expect in principle that the λ_n tend to be smaller as compared to the case when we work with the correct power spectrum, describing the Gaussian distribution function from which the data have been drawn. This should shift the partition function $\Phi(\lambda_n)$ to the left. This fact is known under the name Lilliefors effect and a test taking this into account is the so called Lilliefors test [11].

In this Appendix, we investigate this effect and show that it is negligible in our study. We start by simulating a Gaussian CMB map from the WMAP best fit power spectrum, described by the parameters in table 1.

From this map, we extract the best-fit power spectrum for a Λ CDM model, using a simple χ^2 likelihood in C_ℓ and a simplex algorithm to find its maximum. The theoretical power spectra have been computed with cmbeasy [13].

We then de-correlate the simulated data once with the correct power spectrum and once with the best-fit power spectrum to the simulated data, and plot the empirical partition function of λ_n for both cases. The results are shown in Fig. 12. There is only a very small difference between the two cases, so that we can safely ignore this effect in our analysis.

We assume that this is so because the derived distribution contains only six parameters (the cosmological parameters of the minimal Λ CDM model), which puts a strong prior on

¹⁰http://lambda.gsfc.nasa.gov/product/map/current/m_products.cfm

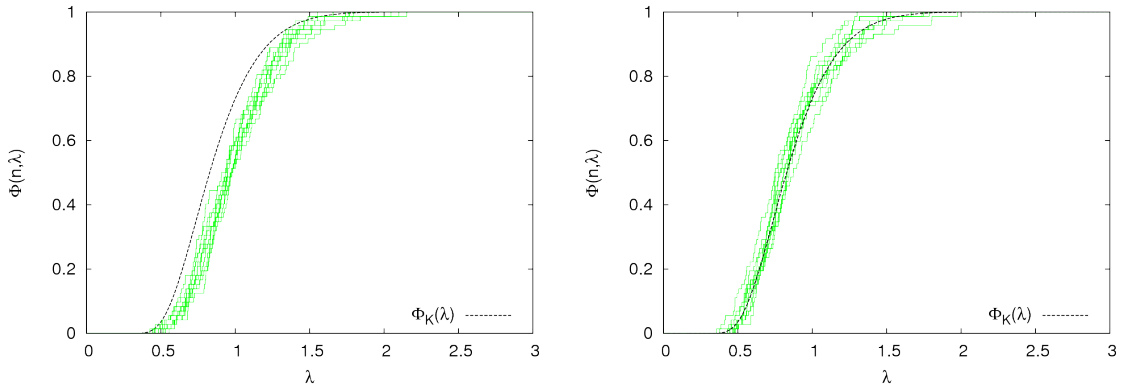


Figure 13. Numerical issues: Empirical partition function of λ_n using (very strongly correlated) neighbouring pixels (*left*), and using every third pixel only (*right*). When we use neighbouring pixels, the curves are biased to higher values of λ_n .

the correlation function, and because it has been derived using many more pixels than the ones used in the Kolmogorov-Smirnov test.

B Numerical issues for very strongly correlated pixels

Very strong correlations between pixels can lead to numerical instabilities in the de-correlation method, as we show in the following. This can be of relevance if the noise in a CMB map is so low that it cannot make up for the missing power on small scales, which is cut by the beam of the experiment. We study these effects with simulated CMB data without noise. We first look at a Healpix-map of $n_{\text{side}} = 512$. The latter has very small pixels (0.013 deg^2) as compared to the WMAP beam (0.048 deg^2 for the W-band and 0.26 deg^2 for the Q-band). Thus, neighbouring pixels are presumably very strongly correlated, resulting in a covariance matrix with eigenvalues close to zero. We therefore expect to run into numerical problems as discussed in Section 2.3. Indeed, when we take into account the WMAP beam, we obtain very small negative eigenvalues, which we think are due to numerical problems in the diagonalization routine. In this case, we cannot take the square-root of the eigenvalue and eq. (2.13) becomes ill-defined.

Even if we do not take into account the beam, but we use all the power up to $\ell_{\text{max}} = 1400$ for both the correlation function and the simulated maps, we do not get a meaningful result. The covariance matrix still has eigenvalues close to zero, which can lead to numerical instabilities in eq. (2.13). We show the effect of this in Fig. 13: Using neighbouring (i.e. strongly correlated) pixels heavily biases the curves, whereas using only every third pixel yields unbiased curves. Not being aware of this effect can lead to wrong conclusions when interpreting the results of the Kolmogorov-Smirnov test. However, we have verified that this effect is no longer present when we add the detector noise of the WMAP experiment to the simulations.

C Finite-size effects

In Section 2.2, we have looked at the effects from small n on the partition function of λ_n , and we found that the the partition function for $n \approx 100$ is already very close to the Kolmogorov-function. In this section, we study the effect from small n in more detail.

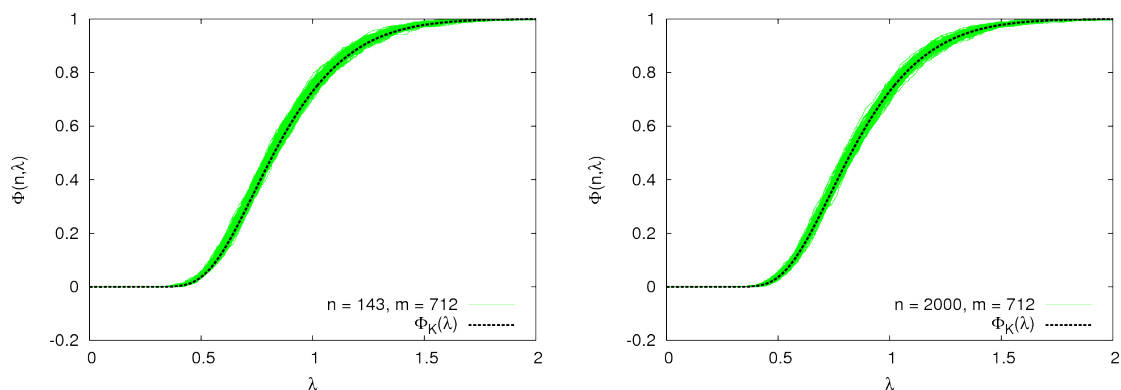


Figure 14. Investigation of effects from small n : *Left panel*: 100 realizations of the empirical partition function of λ_n for $m = 712$ independent ring segments of $n = 143$ pixels each. *Right panel*: Same for $m = 712$ independent ring segments of $n = 2000$ pixels each. The curves for $n = 143$ lie mostly to the left of the Kolmogorov-function, whereas the ones for $n = 2000$ scatter more symmetrically around the latter.

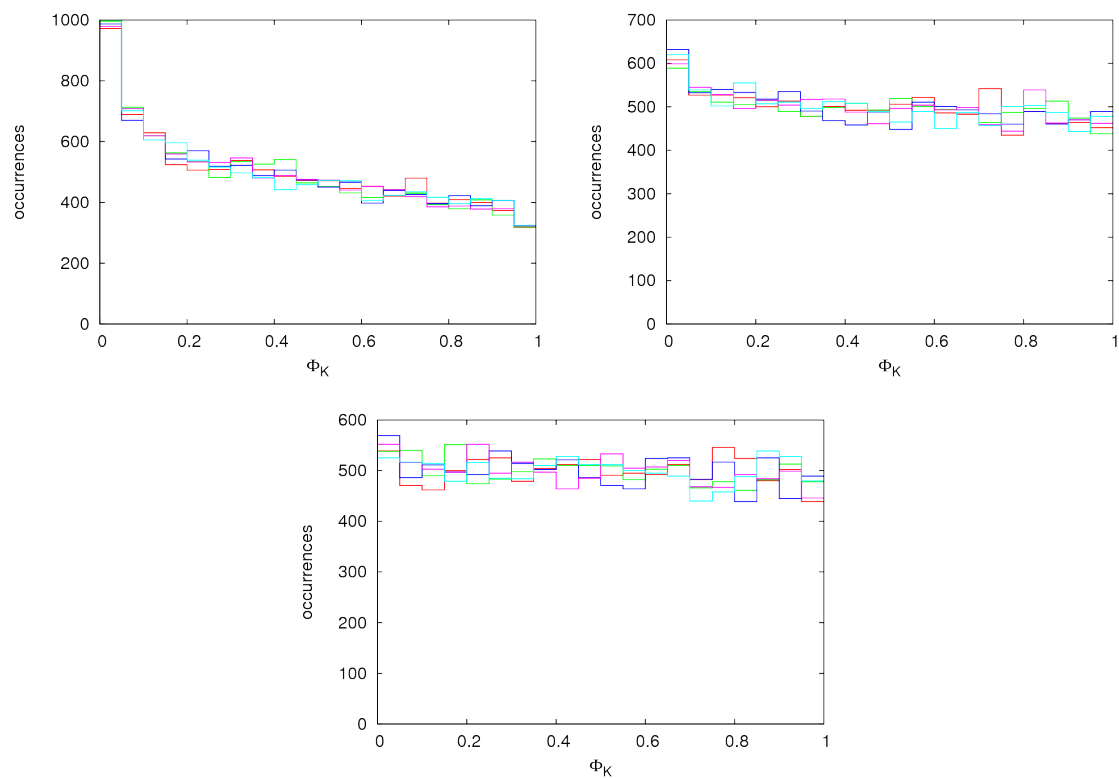


Figure 15. Effects from small n on the histogram of Φ_K . *Upper left*: $n = 10$, *upper right*: $n = 143$, *bottom*: $n = 2000$. For all histograms, we used $m = 10000$, and we show 5 realizations. For $n \rightarrow \infty$, we expect the histogram to be flat.

In Fig. 14, we compare simulations of the empirical partition function of λ_n for $n = 143$ with the one for $n = 2000$. In both plots, we used $m = 712$, which is what we used in the local analysis of WMAP data, and we show 100 realizations of the partition function. For

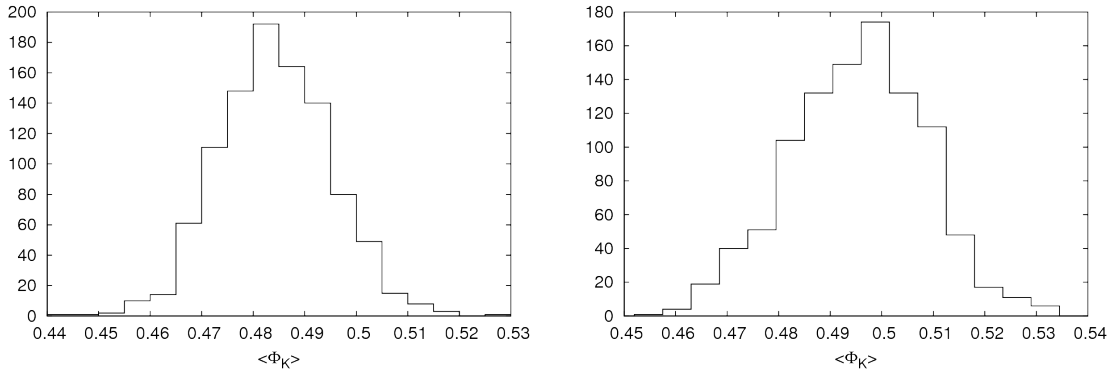


Figure 16. Histogram of $\overline{\Phi_K}$ computed from 1000 realizations. *Left panel:* $n = 143$, $m = 712$. The histogram is centered around 0.484, which means that $\overline{\Phi_K}$ is biased low by about 1.5σ . *Right panel:* $n = 2000$, $m = 500$. The histogram is centered around 0.495, the bias is less than 0.5σ .

$n = 143$, most of the empirical partition functions lie to the left of the Kolmogorov-curve.

The same effect can be seen in Fig. 15, where we show a histogram of all Φ_K for $n = 10$ (upper left), $n = 143$ (upper right), and $n = 2000$ (bottom panel). Here, we have used $m = 10000$ in order to minimize the intrinsic variation of the histogram, and we show 5 realizations. Without finite-size effects, these histograms should be flat, as we argued in Section 3.2.2. The finite-size effect causes a bias of Φ_K towards smaller values.

In order to quantify the resulting bias of $\overline{\Phi_K}$ for our local analysis in Section 3.2.2 ($n = 143$), we compute $\overline{\Phi_K}$ for $n = 143$ and $m = 712$ for 1000 samples, and plot the resulting histogram of $\overline{\Phi_K}$ in the left panel of Fig. 16. We do the same thing for the global analysis in Section 3.3 for $n = 2000$ and $m = 500$, and plot the resulting histogram of $\overline{\Phi_K}$ in the right panel of Fig. 16.

Without the finite-size effects, these should be Gaussian distributed around $\langle \Phi_K \rangle = 0.5$ with a standard deviation of $\sigma = 1/\sqrt{12m} \approx 0.011$ (0.013) for $m = 712$ ($m = 500$), as we have explained in Section 3.2.2. The histogram for $n = 143$ is centered around 0.484 rather than around 0.5, i.e. $\overline{\Phi_K}$ is biased low by about 1.5σ . The histogram for $n = 2000$ is centered around 0.495, i.e. the bias is less than 0.5σ .

D Residual correlations between ring segments and global samples

In Fig. 17, we study the effects of residual correlations between the ring segments and between the global samples. One would expect that these correlations cause the partition functions of λ_n to be too steep as we have argued above. However, in Fig. 17, we verify that for our analyses we do not yet see any effect of this.

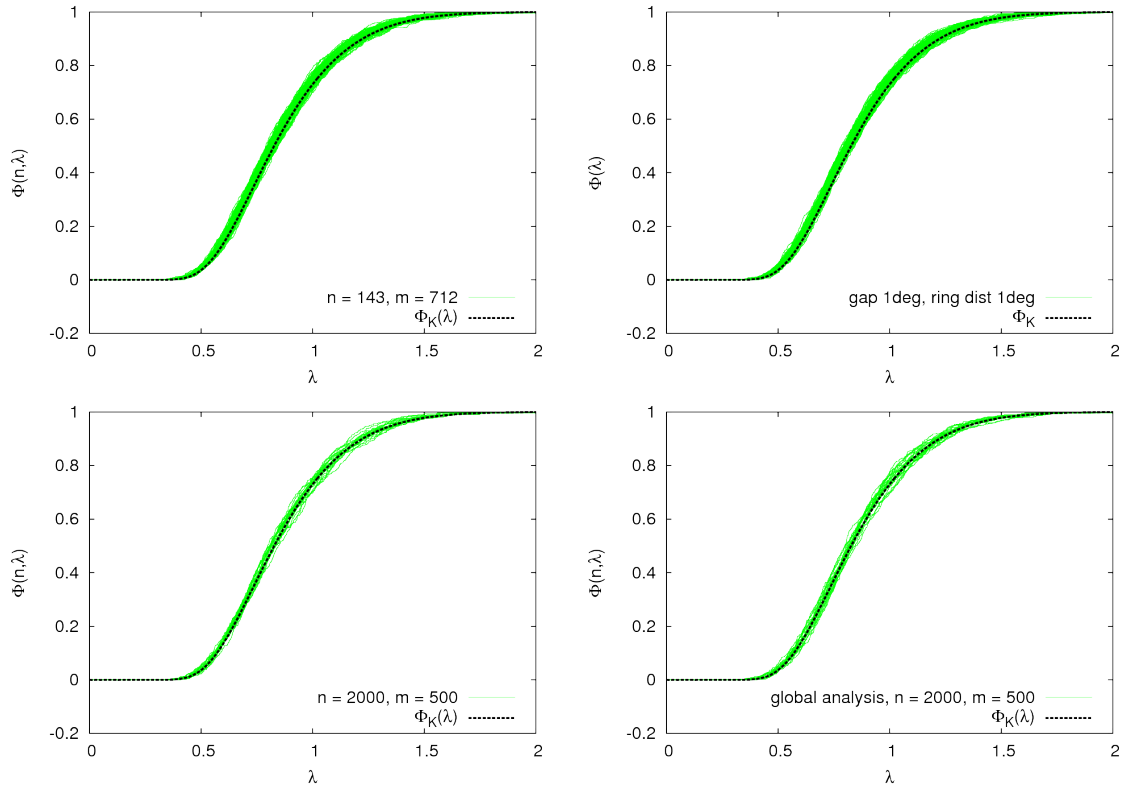


Figure 17. Investigation of effects from correlations between ring segments (*top*) and between samples of the global analysis (*bottom*). In the top (bottom) panels, we show 100 (20) realizations of the simulated empirical partition function of λ_n obtained from the following samples: *Top left:* $m = 712$ independent samples of $n = 143$ pixels each. *Top right:* $m = 712$ ring segments of an opening angle of 20° ($n \approx 143$), and a gap between rings and ring segments of 1° , extracted from simulated CMB maps. *Bottom left:* $m = 500$ independent samples of $n = 2000$ pixels each. *Bottom right:* $m = 500$ global samples of $n = 2000$ pixels each, randomly drawn from simulated CMB maps.

References

- [1] J. Mather et al., *Calibrator Design for the COBE Far-Infrared Absolute Spectrophotometer (FIRAS)*, *Astrophys. J.* **512**, 511 (1999) [astro-ph/9810373];
J. Fixen, *The Temperature of the Cosmic Microwave Background*, *Astrophys. J.* **707**, 916 (2009) [arXiv:0911.1955].
- [2] A.N. Kolmogorov, *Sulla determinazione empirica di una legge di distribuzione*, *G. Ist. Ital. Attuari* **4**, 83 (1933);
V. Arnold, *Orbits' statistics in chaotic dynamical systems*, *Nonlinearity* **21**, T109 (2008).
- [3] R. Durrer, *The Cosmic Microwave Background*, Cambridge University Press (2008).
- [4] V.G.Gurzadyan, A.A.Kocharyan, *Kolmogorov stochasticity parameter measuring the randomness in Cosmic Microwave Background*, *Astron. & Astrophys.* **492**, L33 (2008) [arXiv:0810.3289]
V.G. Gurzadyan et al., *Kolmogorov cosmic microwave background sky*, *Astron. & Astrophys.* **497**, 343 (2008) [astro-ph/0811.2732];
V.G. Gurzadyan et al., *Plane-mirroring anomaly in the cosmic microwave background maps*, *Astron. & Astrophys.* **498**, L1 (2009) [arXiv:0903.3273]

- V.G. Gurzadyan et al., *The power spectrum of the cosmic microwave background Kolmogorov maps: possible clue to correlation of voids*, *Astron. & Astrophys.* **506**, L37 (2009) [arXiv:0909.2162]
- V.G. Gurzadyan et al., *A weakly random Universe?*, *Astron. & Astrophys.* **525**, L7 (2011) [arXiv:1011.3711].
- [5] S.K. Naess, *Application of the Kolmogorov-Smirnov test to CMB data: Is the universe really weakly random?*, arXiv:1105.5051
- [6] J. Michaud, *Test de Komogorov modifié et application au CMB*, Travail de Master Bi-disciplinaire (physique et mathématiques) à l'Université de Genève (2009).
- [7] U. Sawangwit and T. Shanks, *Lambda-CDM and the WMAP power spectrum beam profile sensitivity*, arXiv:1006.1270v1 [astro-ph.CO]
- [8] D. Larson et al., *Seven-Year Wilkinson Microwave Anisotropy Probe (WMAP) Observations: Power Spectra and WMAP-Derived Parameters*, *Astrophys. J. Suppl. Ser.* **192**, 16 (2011) [arXiv:1001.4635].
- [9] M.R. Nolta et al., *Five-Year Wilkinson Microwave Anisotropy Probe (WMAP) Observations: Angular Power Spectra*, *Astrophys. J. Suppl. Ser.* **180**, 296 (2009) [arXiv:0803.0593].
- [10] L. Toffolatti et al., *Extragalactic Source Counts and Contributions to the Anisotropies of the Cosmic Microwave Background. Predictions for the Planck Surveyor mission*, *MNRAS* **297**, 117 (1998) [astro-ph/9711085].
- [11] H. Lilliefors, *On the Kolmogorov-Smirnov Test for Normality with Mean and Variance Unknown*, *Journal of the American Statistical Association* **62**, 399 (1967).
- [12] K.M. Górski et al., *HEALPix – a Framework for High Resolution Discretization, and Fast Analysis of Data Distributed on the Sphere*, *Astrophys. J.* **622**, 759 (2005) [astro-ph/0409513].
- [13] M. Doran, *CMBEASY:: an Object Oriented Code for the Cosmic Microwave Background*, *JCAP* **10**, 011 (2005) [astro-ph/0302138], www.cmbeasy.org.